minerals

MDPI

Article

Dehydroxylation of Kaolinite Tunes Metal Oxide–Nanoclay Interactions for Enhancing Antibacterial Activity

Dongyue Wang [1], Yuhang Meng [1], Aidong Tang [2,3,4] and Huaming Yang [1,2,3,4,*]

[1] Hunan Key Laboratory of Mineral Materials and Application, School of Minerals Processing and Bioengineering, Central South University, Changsha 410083, China
[2] Engineering Research Center of Nano-Geomaterials of Ministry of Education, China University of Geosciences, Wuhan 430074, China
[3] Faculty of Materials Science and Chemistry, China University of Geosciences, Wuhan 430074, China
[4] Key Laboratory of Functional Geomaterials in China Nonmetallic Minerals Industry, China University of Geosciences, Wuhan 430074, China
* Correspondence: hmyang@csu.edu.cn or hm.yang@cug.edu.cn; Tel.: +86-731-88830549

Abstract: Engineered nanoparticle–support interaction is an effective strategy for tuning the structures and performance of engineered nanoparticles. Here, we show that tuning the dehydroxylation of kaolinite nanoclay as the support could induce zinc oxide–kaolinite interactions. We used free energy theory, electron microscopy, and X-ray photoemission spectroscopy to identify interaction strengths between metal oxides and the underlying nanoclay induced by dehydroxylation. Desirable exposure of nanoparticle sites and the geometrical and crystal structure were obtained by tuning the interface interactions between ZnO nanoparticles and nanoclay. The surface free energy of zinc oxide–nanoclay results in different interfacial interactions, and the properties of the surface free energy electron-donating (γ^-) and electron-accepting (γ^+) parameters have significant effects on the electron acceptor. This could, in turn, promote stronger interactions between zinc oxide and the kaolinite surface, which produce more active (0001) Zn-polar surfaces with promoting zinc oxide nanoparticles growing along the <0001> direction. Reactive oxygen species, leached zinc ions, and electron transfer can modulate the antibacterial activities of the samples as a function of interface free energy. This further demonstrates the interfacial interactions induced by dehydroxylation. This work has new application potential in biomedicine and materials science.

Keywords: kaolinite; dehydroxylation; interfacial interactions; ZnO nanoparticles; antibacterial activities

check for updates

Citation: Wang, D.; Meng, Y.; Tang, A.; Yang, H. Dehydroxylation of Kaolinite Tunes Metal Oxide–Nanoclay Interactions for Enhancing Antibacterial Activity. *Minerals* **2022**, *12*, 1097. https://doi.org/10.3390/min12091097

Academic Editor: Francisco Franco

Received: 2 August 2022
Accepted: 25 August 2022
Published: 29 August 2022

Publisher's Note: MDPI stays neutral with regard to jurisdictional claims in published maps and institutional affiliations.

Copyright: © 2022 by the authors. Licensee MDPI, Basel, Switzerland. This article is an open access article distributed under the terms and conditions of the Creative Commons Attribution (CC BY) license (https://creativecommons.org/licenses/by/4.0/).

1. Introduction

Engineered nanoparticles (ENPs) have been extensively investigated and applied in various fields such as energy, the environment, sensors, and biomedicine due to their enhanced physical/chemical properties [1]. Metal oxides are one type of ENPs and are the crucial and functional component in engineered nanoparticle applications [2]. Versus other metal oxide NPs, ZnO NPs have excellent medical activity because they can generate intracellular reactive oxygen species (ROS) and release zinc ions [3–5]. The crucial parameters to enhance the medical performance of ZnO NPs are dependent on particle size, morphological characteristics, crystal plane, crystal orientation, and surface defects [6,7]. Their activities are tuned via particle size, morphology, and crystal structure through appropriate synthesis methods [8]. The design and control of ZnO NPs' properties, such as their size, morphonology crystal orientation, surface defects, and style planes, can promote unique properties and performance [9,10]. Therefore, constructing the proper nanoparticle–support interactions to enhance the solubility of ZnO NPs or develop extracellular ROS is a desirable strategy.

Nanoparticles are often anchored onto supports that increase the active sites and stabilize the nanoparticles [11–13]. Different strategies and designs have been developed

to anchor the nanoparticles on the support and increase nanoparticle activity [14–17]. The nanoparticle–support interactions lead to unique nanoparticle properties including size, shape, and structure—these strongly influence their performance [18–21]. Despite the various design strategies seen in these advanced supports, some issues remain to be addressed [22]. First, the hazardous agents used in the synthesis of the supports can lead to irreversible destruction of the metal oxide–support interfaces with accompanying reductions in stability [23]. In addition, high temperature is often used to create interface interactions, thus leading to thermodynamically unstable nanoparticles that often aggregate or undergo Ostwald ripening. Additional steps are then required under harsh conditions to re-expose the active sites [24]. Achieving a high loading content and avoiding self-agglomeration is another major challenge. Current methods cannot be applied on a large scale and are hampered by high cost and low yields [25]. It is highly desirable to increase the specific surface area of the supports and increase the number of anchoring sites. Therefore, a general and gentle synthetic strategy that can stabilize a broad range of engineered nanoparticles with tuning metal oxide–support interfaces is urgently needed.

Various supports have been indicated to significantly affect the performance of engineered nanoparticles by changing the nature of the metal oxide-O–support bond in the surface structure. Among numerous support materials, alumina (Al_2O_3) and silica (SiO_2) are supposed to be a class of prominent support candidates due to their inert nature, low cost, and large surface area. Mentasty prepared a series of chromium oxide supported on different Al_2O_3 supports toward propane dehydrogenation. The results showed that the Al_2O_3 support with high specific surface had a strong chromium–support interaction, which affected the information of polymeric species [26]. In addition, it has been found that the change in metal oxide ratio was caused by the interactions between species and different supports. The surface of the alumina support was covered by abundant hydroxyl groups, which give rise to stronger nanoparticles–support interactions. More importantly, the nanoparticles–support interactions were revealed to play a crucial role in the distribution, oxidation state, reducibility, and acid base properties of doped species. The amount and nature of surface hydroxyl groups of supports (Al-OH and Si-OH) induce the different interactions between chromium species and support, which generates an exceedingly support-dependent dispersion, oxidation states, reducibility, and acid-base properties for the prepared nanoparticles performance.

Kaolinite ($Al_2Si_2O_5(OH)_4$) is one example of a two-dimensional material formed by stacking Al–O octahedral and Si–O tetrahedral structures. This clay mineral has been widely used to assemble functional nanoparticles due to its low cost, large surface area, and high stability. The abundant hydroxyl groups and permanent negative charge of kaolinite prevents the self-agglomeration of metal oxide nanoparticles [22]. Moreover, the oxygen vacancies of the kaolinite surface can remove hydroxyl groups and construct more reactive and anchoring sites for oxides [27–29]. The nature of surface O vacancies and the number of −OH groups can both be tuned by dehydroxylation. The abundance of hydroxyl groups and O vacancies on the clay surface can be adjusted, and this strategy can enhance its performance and broaden its applications. The nature of the surface O vacancies and the amount of −OH groups can both be tuned by dehydroxylation. Hydroxyl groups on the surface of kaolinite can produce/maintain interactions between nanoparticles while simultaneously generating oxygen vacancies on the kaolinite surface to enhance the nanoparticles' properties. Therefore, anchoring ZnO nanoparticles on the surface of kaolinite is an efficient method to produce/maintain metal oxide dispersion via −OH groups on the support. This strategy can simultaneously generate oxygen vacancies near the nanoparticle sites [30]. The O vacancy can be formed via high-temperature treatment. The density of these vacancies on the support surface may be adjusted by changing the annealing temperature. Accordingly, the amount and nature of surface hydroxyl natural minerals have been extensively utilized as supports due to their stable physical–chemical properties [31]. This strategy is expected to be an efficient approach that broadens the use of ZnO NPs in biomedical fields.

Here, we report that the morphology, size, and crystal properties of zinc oxide nanoparticles can be tuned and anchored via interface interactions induced by the dehydroxylation of the kaolinite surface. The strong interactions between the support and active nanoparticles motivated us to develop alternative methods to promote the activities of zinc oxide. Importantly, the interface characteristics of the zinc oxide and the support suggest that the zinc oxide–support interaction has significant effects on the morphology, size, crystal lattice distance, and crystal orientation. Further investigations demonstrate that the surface free energy of zinc oxide–support results in different interfacial interactions. The properties of the support's surface free energy have significant effects on the interfacial interactions. The zinc oxide nanoparticles dissolve, thus mediating their activity. Indeed, ROS, leached zinc ions, and electron transfer mediate the antibacterial activities and lead to trends in interface free energy. This further proves the interfacial interactions induced by dehydroxylation. Our results can help circumvent the current limits of approaches involving strong chemical reagents while concurrently obtaining various nano structural zinc oxide nanoparticles, which could lead to opportunities to rationally maneuver structure-dependent biomedical outcomes.

2. Materials and Methods

2.1. Materials and Synthesis

Kaolinite (Kaol) powders were purchased from Sigma-Aldrich (St. Louis, MO, USA), and the composition of medical kaolinite is shown in Tables S1 and S2. Fluorescein isothiocyanate, dimethyl sulfoxide, 5,5-dimethyl-1-pyrroline-N-oxide, XTT (2,3-bis(2-methoxy-4-nitro-5-sulfophehyl)-2H-tetrazolium-5-carboxanilide), and methanol were obtained by Aladdin (Shanghai, China). Hoechst was purchased from the Beyotime Institute of Biotechnology (Shanghai, China). All reagents were used as received without further purification. Zinc acetate dihydrate ($Zn(CH_3COO)_2{\cdot}2H_2O$, AR, 99%), ethanol ($CH_3CH_2OH$, GC, 99.9%), ammonium hydroxide solution (H_5NO, 18 wt.%), and kaolinite were obtained from Aladdin. The DI water used in the catalyst preparation was from local sources. All reagents were used as received without further purification.

Zinc acetate dihydrate ($Zn(CH_3COO)_2{\cdot}2H_2O$, AR, 99%), ethanol ($CH_3CH_2OH$, GC, 99.9%), ammonium hydroxide solution (H_5NO, 18 wt.%), and kaolinite were obtained from Aladdin. The DI water used in the catalyst preparation was from local sources. Here, 1 g of kaolinite was added to 60 mL of alcohol aqueous solution (V ethanol:V water = 1:1) and was ultrasonically dispersed at room temperature to form a kaolinite suspension. Subsequently, 0.4 g of Zn $(AC)_2{\cdot}2H_2O$ was added and stirred at room temperature. After the aging reaction for 2 h, the $NH_3{\cdot}H_2O$ solution with a concentration of 1 mol/L was slowly added to the above mixture until the pH was 8 and then aged for 2 h. The reaction products were washed centrifugally with ethanol and deionized water, dried at 60 °C, and then calcined at 250 °C (ZK250), 300 °C (ZK300), 350 °C (ZK350), 400 °C (ZK400), and 450 °C (ZK450) for 4 h; the heating rate was 5 °C/min. The powder was ground to obtain the product ZnO/kaolinite composite catalytic material. As a control, pure zinc oxide nanoparticles were similarly prepared but without kaolinite.

2.2. Characterization

Powder X-ray diffraction (XRD) measurements were recorded on a Bruker D8 Advance (Bruker Corporation, Saarbrücken, Germany) operating at 40 mA and 40 kV with Cu Kα radiation. TGA used a STA449C instrument at an airflow of 60 mL/min and a heating rate of 5 °C/min. Fourier transform infrared (FTIR) analysis of the samples was conducted with a FTIR spectrophotometer (Scientific Nicolet 6700, Thermo Electron Corporation, Waltham, MA, USA) between 4000 and 400 cm^{-1}. SEM images were taken on a JEOL JSM-7001F (JEOL, Tokyo, Japan) field emission scanning electron microscope. HRTEM images, EDX, and elemental mapping images were obtained on EM-ARM300F electron microscope (JEOL, Japan). Atomic force microscopy (AFM) (Bruker Dimension ICON, Bruker Corporation, Saarbrücken, Germany) was used to analyze the surface roughness

and surface potentials. X-ray photoelectron spectroscopy (XPS) studies were carried out on an ESCALAB 250 (Thermo Scientific, Waltham, MA, USA) using an Al Kα monochromated source (hv = 1486.6 eV). Spectra were analyzed using Thermo Scientific Avantage software (Version 5.52, Thermo Scientific, Waltham, MA, USA). All of the binding energies were calibrated by the C 1s peak at 284.6 eV. The UV-vis absorption spectra were recorded on a PE, Lambda1050 UV-vis spectrophotometer. EPMA spectra were recorded on JXA-8530F PLUS (JEOL, Tokyo, Japan). STEM and EDX analyses operating at 200 kV were fitted with a Nikon aberration corrector and an Oxford Instruments INCA TEM 300 system (Thermo Scientific, Waltham, MA, USA). The oxygen vacancies in solid samples were measured with a Bruker EMXPLUS electron paramagnetic resonance instrument (EPR, Bruker EMXplus-6/1, Bruker Corporation, Saarbrücken, Germany).

2.3. Antibacterial Species Measurements

EPR spectroscopy (EPR, Bruker EMXplus-6/1, Bruker Corporation, Saarbrücken, Germany) used 5,5-dimethyl-1-pyrroline-N-oxide as a spin trap to detect ROS. Here, 100 μM XTT (2,3-bis(2-methoxy-4-nitro-5-sulfophehyl)-2H-tetrazolium-5-carboxanilide) was used as the indicator. The 5.25 mM XTT stock solution was at 4 °C. After incubation for 1 h, 2 h, 3 h, 4 h, and 5 h, respectively, the suspension (1 mL) was sampled and injected into a quartz vial. The concentration of the orange-colored XTT-formazan was measured using a UV-vis spectrophotometer at 470 nm. Dissolution experiments of samples were collected after culturing without bacteria at 37 °C for 1 h, 2 h, 3 h, and 4 h. The amounts of Zn^{2+} in the solution were determined quantitatively by inductively-coupled plasma mass spectroscopy (ICP-MS, Agilent 7700, Agilent Technologies Inc., Santa Clara, CA, USA). Electrochemical characterization was performed with a single-chamber, three-electrode system to monitor the electrochemical behavior of samples after 4 h incubation. Here, 100 μL of the bacteria–materials solution was dropped onto the sample surface and dried at 37 °C to form the bacteria film. Cyclic voltammetry (CV) and the current–potential (I–V) curves were conducted on a CHI660E instrument in a potential range of –0.5 to 0.5 V with a scan rate of 0.05 mV/s. for 0.5 h. The antibacterial activity of ZnO–kaolinite samples was assessed with Gram-negative (*E. coli*, ATCC 25922) bacteria. In brief, the pure bacteria in LB were cultivated overnight in a rotating shaker at 37 °C. The bacteria solution was prepared for the antibacterial test and was diluted and spread on agar plates for CFU analysis after 4 h of treatment.

2.4. Surface Free Energy Calculation

The contact angles experiments were carried out five times, and the average values were presented. The total surface free energy γ is composed of two parts: the nonpolar part γ^{LW} (i.e., Lifshitz–van der Waals) and the polar part γ^{AB} (i.e., Lewis acid-base) according to the van Oss–Chaudhury–Good theory [32,33]. The non-polar dispersive component is mainly attributed to London forces, while the polar component (Lewis acid-base interactions) is mainly associated with hydrogen bonding and the behavior of the electron donor-acceptor (i.e., γ^- and γ^+). The surface free energy of the solid γ^S and the liquid γ^L can be calculated as:

$$\gamma_S = {\gamma_S}^{LW} + {\gamma_S}^{AB} = {\gamma_S}^{LW} + 2\sqrt{{\gamma_S}^+{\gamma_S}^-} \quad (1)$$

$$\gamma_L = {\gamma_L}^{LW} + {\gamma_L}^{AB} = {\gamma_L}^{LW} + 2\sqrt{{\gamma_L}^+{\gamma_L}^-} \quad (2)$$

According to the Dupre equation, the solid–liquid interfacial free energy γ^{SL} is expressed as:

$$\gamma_{SL} = \gamma_S + \gamma_L - 2(\sqrt{{\gamma_S}^{LW}{\gamma_L}^{LW}} + \sqrt{{\gamma_S}^+{\gamma_L}^-} + \sqrt{{\gamma_S}^-{\gamma_L}^+}) \quad (3)$$

By combining Equations (1)–(3) and Young's equation, Equation (4) is obtained:

$$(\gamma_L{}^{LW} + 2\sqrt{\gamma_L{}^{+}\gamma_L{}^{-}})(1+\cos\theta) = 2(\sqrt{\gamma_S{}^{LW}\gamma_L{}^{LW}} + \sqrt{\gamma_S{}^{+}\gamma_L{}^{-}} + \sqrt{\gamma_S{}^{-}\gamma_L{}^{+}}) \quad (4)$$

Based on Equation (4), the solid surface energy and its components can be obtained by measuring the contact angles of three different liquids (two polar liquids are required).

2.5. Morphological Observation of Bacteria

A glutaraldehyde solution (2.5%) was used to fix the bacteria overnight, and the samples were dehydrated with ethanol solutions (30, 50, 75, 90, 95, and 100%) sequentially and vacuum-dried. The morphological images of the bacteria were acquired by SEM and TEM. Each group contained three parallel samples, and at least two sets of images were acquired from each sample.

3. Results and Discussion

3.1. Characterization of ZK Samples

The synthetic details of the materials are described in Section 2: Materials and Methods. Briefly, the $Zn(OH)_2$/kaolinite precursor was synthesized through a solution method via a mixture of kaolinite, $Zn(Ac)_2{\cdot}2H_2O$, and $NH_3{\cdot}H_2O$ followed by an aging reaction (Figure S1). Zinc oxide nanoparticles were then obtained on the surface of kaolinite via calcination at various oxidation temperatures (Figures S2 and S3). The precursor can nucleate on the kaolinite surface, leading to the interaction between nanoparticles and the kaolinite support. For comparison, ZnO was similarly synthesized without adding kaolinite. This control was used to compare the antibacterial activity between the zinc oxide and ZnO/kaolinite. X-ray diffraction (XRD) determined the crystal structure and crystallization degree (Figure S4). The XRD patterns of ZK250, ZK300, ZK350, ZK400, and ZK450 show that all samples are crystalline, with characteristic peaks at $2\theta = 32^\circ$, 35°, and 37°. These can be assigned to the (100), (002), and (101) peaks of zinc oxide according to the standard PDF card, respectively (JCPDS/ICDD 36-145); the characteristic peaks at $2\theta = 12.3^\circ$ and 25° can be assigned to the (001) and (002) lattices of kaolinite, respectively, according to the standard PDF card (JCPDS card no. 14-0164). In the XRD patterns of ZnO/kaolinite, the intensity of the (001) and (002) kaolinite peaks as well as the (100) and (002) ZnO peaks first decreases and then increases with oxidation temperature (Figure S4a). This indicates that dehydroxylation of the support surface has a significant effect on the crystal structure of the zinc oxide nanoparticles. The degree of crystallinity was calculated based on the XRD patterns. The degree of kaolinite crystallinity decreases while the degree of ZnO crystallinity increases (Figure S4b), suggesting the presence of metal oxide–support interactions. There was a difference in surface dehydroxylation induced by the different interactions between the zinc oxide and support (Figures S5 and S6). The XRD pattern characterization suggests that dehydroxylation mediates the crystal structure of the oxide and the support and promotes crystallization of ZnO/kaolinite to ultimately facilitate zinc oxide–support interactions.

3.2. Interface Formation of Zinc Oxide Nanoparticles on the Kaolinite Surface

We used scanning electron microscopy (SEM) and high-resolution transmission electron microscopy (HRTEM) in combination with atomic force microscopy (AFM) and electron probe microanalysis (EPMA) to understand the morphology and microstructure of zinc oxide nanoparticles. The SEM and TEM observations reported below are general findings suggesting that zinc oxide nanoparticles distribute uniformly and stably on the substrate surface (Figure S7). Figure 1a shows the different nanoparticle morphologies and sizes observed with the increasing extent of dehydroxylation. The contact area between nanoparticles and the support surface shows different states: ZK350 exhibits a structural shape of a sphere with a clear contact board, while other samples are hemispherical. The yellow dashed lines represent the board of nanoparticles, and the green dashed lines represent

the kaolinite surface, suggesting that different zinc oxide–support interactions are induced by hydroxylation. The HAADF images show that the crystal structure has an interplanar distance of 0.13 nm for ZK250, ZK300, and ZK450 and 0.15 nm for ZK350. Furthermore, the crystal orientation of ZK350 has a vertical direction toward the support surface (white line), while other samples have a lower angle between the crystal orientation and the support surface. These observations suggest that the zinc oxide–support interactions could change the geometrical and crystal structure. The change of crystal orientation indicates that the interactions change the exposed crystal planes and have a significant effect on the reactive surface of the ZnO nanoparticles. The crystal orientation changed (red arrow) due to the extent of dihydroxylation.

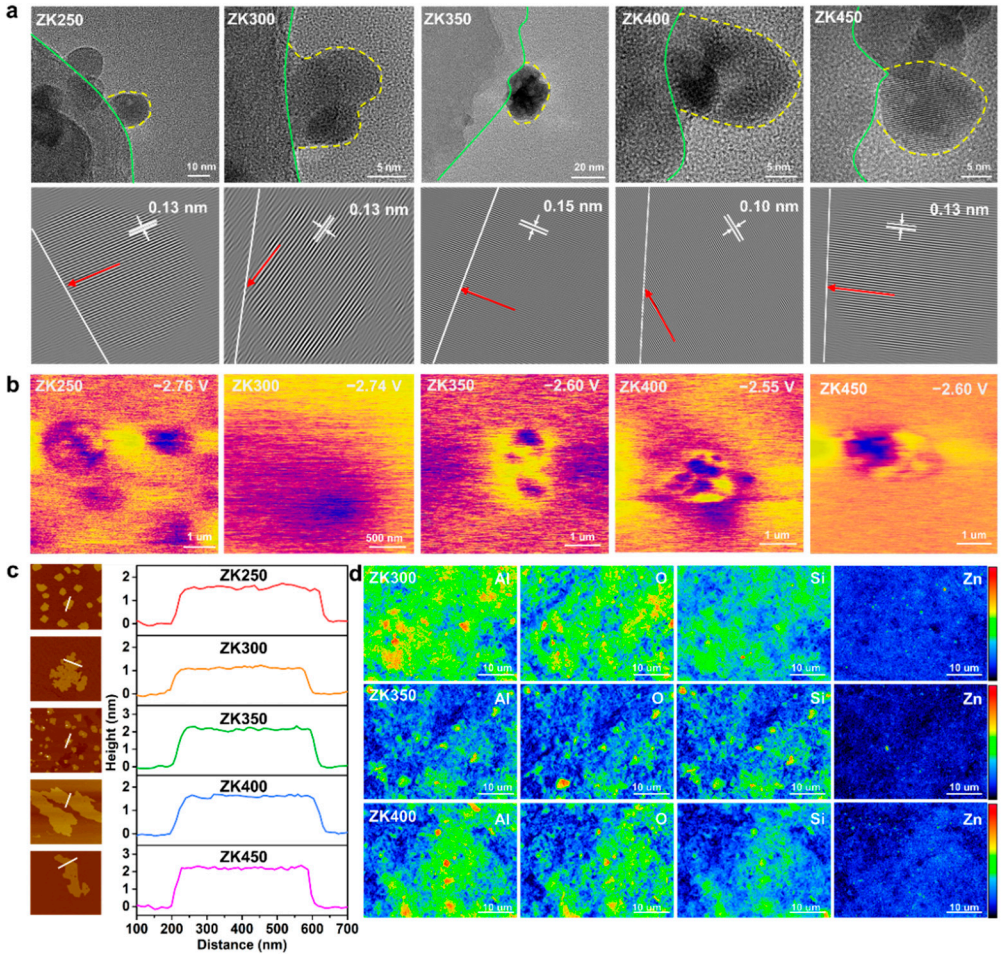

Figure 1. (**a**) HRTEM image; the yellow dot line indicates the border of the nanoparticles, and the green line represents the border of the support. HAADF images of ZnO nanoparticles on the support surface. The white line represents the border of the surface, and the red arrows illustrates the crystal lattice orientation; (**b**) Surface electronic chemical potential distribution; (**c**) The heights of ZnO on the support by AFM; (**d**) Intensity and distribution of Al, Si, O, and Zn of EMPA.

The KPFM results show that ZK400 has a higher electronic chemical potential of −2.55 V, while ZK350 and ZK4500 are lower, with potentials of −2.60 V. ZK400 and ZK450 exhibit similar electronic chemical potentials of −2.6 V, which are attributed to the oxygen vacancies (Figure 1b). The surface potential distributions indicate that the dehydroxylation not only affects the zinc oxide–support interactions but also changes the surface potential distribution, which could cause potential differences to accelerate electron transfer between the samples and bacteria cells. AFM imaging was also performed to further assess the nanoparticles' morphology [34]. The AFM images show that the height of ZK350 was twice that of ZK300, and the heights of ZK250, ZK400, and ZK500 have a similar trend

consistent with SEM results (Figures 1c and S8). Here, the height of ZK350 is the highest, and the heights of ZK300 and ZK400 are lower than ZK350, further proving that the zinc oxide–support interactions could change the geometrical structure.

EPMA was performed to detect the intensity of different elements of the surface (Figure 1d). EMPA mapping shows that ZK350 exhibits more blue or dark areas and less red or bright areas for all elements including Al, Si, O, and Zn. The results suggest that the ZK350 surface was more stable, and the total surface energy of ZK350 was lower than ZK300 and ZK400. The lower surface activity of ZK350 decreases the "hot spots" on the surface and results in a lower intensity signal. Therefore, surface interactions not only change the crystal structure and the contact area but also have significant effects on surface energy. This analysis further illustrates that zinc oxide–support interactions have significant effects on the surface property. In addition, Table S3 shows that the intensity ratio $I_{(100)}/I_{(002)}$ increased with dehydroxylation. A small $I_{(100)}/I_{(002)}$ ratio indicates the formation of zinc oxide nanoparticles oriented along the c-axis with (0001) or (0001) end faces. The high $I_{(100)}/I_{(002)}$ ratio indicates zinc oxide nanoparticles shortening along the c-axis, as well as an increased proportion of the (0001) and (0001) polar faces. The interfacial interactions can promote the oriented growth of zinc oxide nanoparticles along the a-axis (<1000> direction), thereby increasing the proportion of polar faces. The characteristics of the zinc oxide and support suggest that zinc oxide–support interactions have significant effects on the morphology, size, crystal lattice distance, and crystal orientation toward the surface of the substrate. This results in different surface properties including the surface activities, surface potential, and surface free energy. The effective and reactive surface area of the nanoparticles can affect their solvent and can have negative effects on the dissolution of ZK350 and production of active oxygen species.

3.3. Interfacial Interaction Analysis and Calculations of ZK Samples

The coordination environment of the ZnO/kaolinite structure was studied to further understand the zinc oxide–support interaction induced by dehydroxylation. The X-ray photoelectron spectroscopy (XPS) results show that the binding energy of Al, Si, and O all shifted to higher binding energy following the increase in oxide temperature from 250 °C to 300 °C (Figure S9); however, the binding energy of all these elements shifts back to a lower binding energy at 350 °C, suggesting that the coordination environment of ZK350 is more stable than other samples. Moreover, a more stable interaction was formed at the ZnO and kaolinite interface [35–37]. The binding energy of Al, Si, and O was reversed after 350 °C oxidation, returning to a higher binding energy and demonstrating that the coordination environment is unstable relative to ZK350. The binding energy peak shifts for Al, Si, and O demonstrate that the electron structure perturbation has different interaction formations at their interface. The Al, Si, and O binding energy peaks of ZK350 were lower than other samples, suggesting that the zinc oxide–support interaction is strong and stable. Meanwhile, the binding energy peak of Zn shifted from a higher binding energy to a lower binding energy as the oxidation temperature increased, suggesting that the coordination environment was affected by dihydroxylation, which indicates that different zinc oxide–support interactions exist at the interface.

The surface free energy was calculated to investigate the origin of different interaction formations at the zinc oxide–support interface (Table S4). The physical properties of nanoparticles are greatly affected by the surface free energy of the substrate, i.e., the crystal structure, morphology, growth mode of nanoparticles, and lattice mismatch [38,39], and hence, surface free energy, including total surface free energy, polar surface free energy, Lifshitz–van der Waals free energy, Lewis base and acid free energy, and adhesion free energy. The total surface free energy (Figure 2a), polar surface free energy γ^{AB} (Figure 2b), and Lifshitz–van der Waals free energy γ^{LW} (Figure S10a) increases with dihydroxylation; comparatively, the surface free energy components of ZK350 are the largest, and the surface free energy decreases with increasing dehydroxylation. These results suggest that the zinc oxide nanoparticles could anchor strongly and form a stable interaction on the ZK350

interface. The acid-base components of electron-donating γ^- parameters (Figure S10b) and electron-accepting γ^+ parameters (Figure 2c) were separated from γ^{AB}. The Lewis acid surface free energy γ^+ results illustrate that ZK350 has a better electron acceptor and could promote stronger interactions between the zinc oxide and kaolinite surface because the surface can accept donated electrons to influence the adsorption of zinc. Furthermore, the Lewis base free energy γ^- of ZK350 exhibits a lower energy that cannot influence the interaction. These trends are consistent with the XPS results. Thus, the highest surface free energy of the zinc oxide–support results in the highest interfacial interactions. The lowest surface free energy exhibits the lowest interfacial interactions, and the properties of the support surface free energy have significant effects on the interfacial interactions.

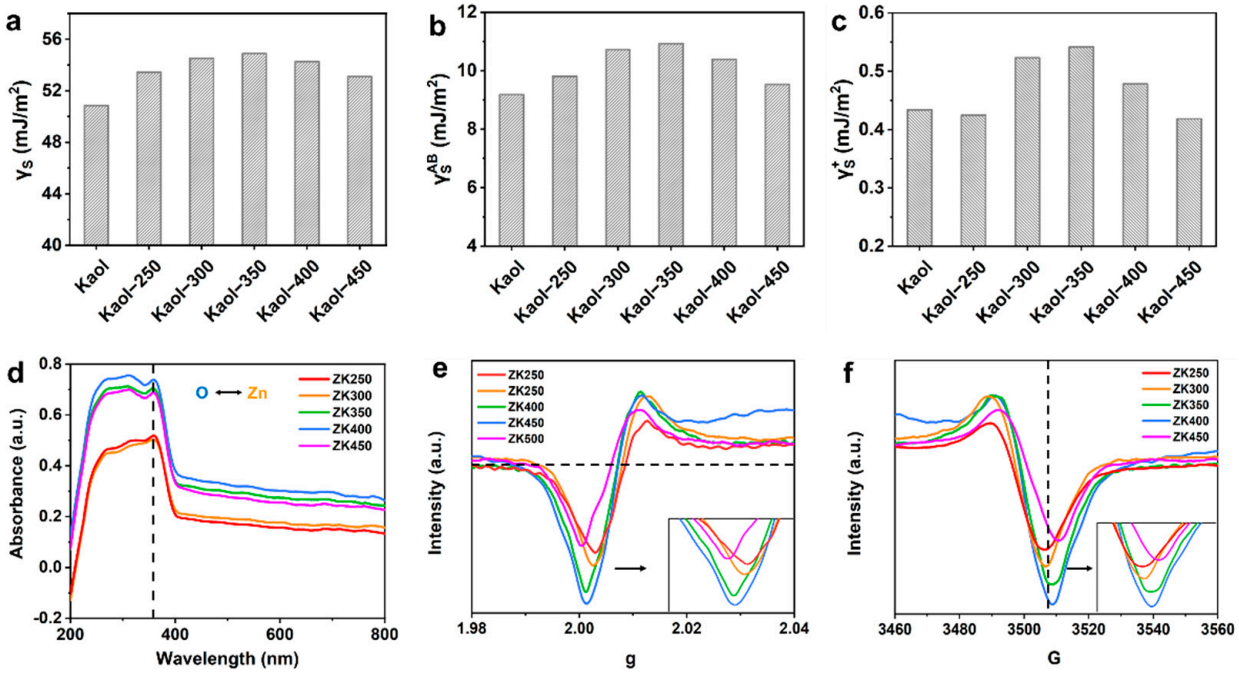

Figure 2. Surface free energy including: (**a**) total surface free energy; (**b**) polar surface free energy and (**c**) Lewis acid surface free energy; (**d**) UV-vis spectra (the black arrow represents the electron transfer between O 2p and Zn 2p). EPR spectra of (**e**) g and (**f**) G of the samples.

The surface free energy and interfacial free energy are affected by the dehydroxylation of support, and, thus, the UV-vis spectra and the electron paramagnetic resonance (EPR) were analyzed to study the electron transfer [17,40]. The electron transfer process in the interface between zinc oxide and support was further verified by the UV-vis absorption spectra (Figure 2d). The strong absorption peak at 359 cm^{-1} was attributed to the charge-transfer transition from the O 2p to the Zn 2p orbital—this is consistent with the XPS results for Zn binding and the energy peak shift. The absorption peak intensity of samples becomes stronger with increasing dehydroxylation extent, which indicates that the charge-transfer transition becomes strong. Meanwhile, the reinforced peak intensity indicates that the support facilitates the information of ZnO phases, which is in accordance with the XRD results. Thus, this fact has proved that the coordination state of Zn species can be affected by the nature of support. Moreover, the trend indicates that there are more surface oxygen vacancies in the samples as dehydroxylation increases, which is consistent with the FTIR results and the results that the production of hydroxyl radicals increase with dehydroxylation due to the increase in oxygen vacancies. Oxygen-vacancy-sensitive EPR experiments were also carried out (Figure 2e,f), and there is a higher peak intensity at g = 2, which suggests that the concentration of oxygen vacancies increases, and more oxygen vacancies form at the material surface. Moreover, the peak of the EPR signal becomes stronger with increasing dihydroxylation, thus demonstrating that electrons are trapped in

oxygen vacancies in or around the interface [41,42]. Thus, the surface free energy of zinc oxide–nanoclay results in different interfacial interactions, and the properties of the surface free energy electron-donating (γ^-) and electron-accepting (γ^+) parameters have significant effects on the electron acceptor. This could, in turn, promote stronger interactions between zinc oxide and the kaolinite surface, which promote the increase in the (0001) Zn-polar surface and a decreased proportion of nonpolar surfaces.

3.4. Morphology Characteristics during Dissolution of Zinc Oxide Nanoparticles

The interfacial interactions and morphology were further investigated by spherical aberration-corrected electron microscope electron microscopy (STEM) [43,44]. ZnO nanoparticles are anchored on the support with a larger contact area and a clear board for ZK300 while ZK300 exhibits a smaller contact area (Figure S11). The EDS elemental mapping shows that the Al, Si, O, and Zn of samples are uniformly distributed on the surface. However, the Al and Si element of ZK350 migrates from the support surface to the zinc oxide surface, and the Al and Si signal intensities in the zinc oxide nanoparticles become stronger than those of ZK300, demonstrating that the interface interaction induced by dihydroxylation becomes stronger. The surface potential distributions indicate that the dehydroxylation not only affects the zinc oxide–support interactions but also changes the surface potential distribution, which could promote electron transfer between the surface of the samples and the bacteria cells. These details are confirmed in the antibacterial activity section. The STEM images also show that ZK350 ZnO nanoparticles are anchored on the support with a contact area and a clear board while ZK300 exhibits a smaller contact area. The characteristics of the interface contacts are consistent with Figure 4b. The EDS elemental mapping shows that the Al, Si, O, and Zn of samples are uniformly distributed on the surface. With increasing dehydroxylation, the Al and Si element ZK350 migrates from the support surface to the zinc oxide surface, and the Al and Si signal intensities in the zinc oxide nanoparticles become stronger than those of ZK300, demonstrating that the interface interaction induced by dihydroxylation becomes stronger. The results of the elemental distribution on the surface are consistent with XPS results; the interface interactions of ZK350 are stronger than other zinc oxide–support samples.

The morphology characteristics of zinc oxide nanoparticles during the dissolution are affected by the inter-surface properties of nanoparticles and support [45,46]. To study the effects of interface interactions on the dissolution of zinc oxide nanoparticles, the morphological properties of the nanoparticles were investigated by HRTEM during dissolution (Figure 3). The border of the ZK300 nanoparticles becomes vague with a longer dissolution time. After 3 h, the surface of the zinc oxide in ZK300 gradually becomes vague (yellow arrows). The board and morphology of ZK300 nanoparticles were illustrated by red dash line and blue arrows in Figure 3a. In contrast, the ZK350 zinc oxide nanoparticles' surface has no obvious observations during the dissolution process. The zinc oxide nanoparticles of ZK350 maintain a clear border and maintain the same morphology (as shown in red arrows). The board and morphology of ZK350 nanoparticles were illustrated by red dash line and blue arrows in Figure 3b. The different dissolution characteristics of the zinc oxide nanoparticles demonstrate that different reactive surfaces of the zinc oxide nanoparticles are exposed to the solution. Furthermore, the dissolution properties of the zinc oxide nanoparticles suggest that the reactive surfaces of the zinc oxide nanoparticles are affected by zinc oxide nanoparticle–support interface interactions. Thus, the results reveal that interface interactions induced by dehydroxylation could affect the dissolution of zinc oxide nanoparticles.

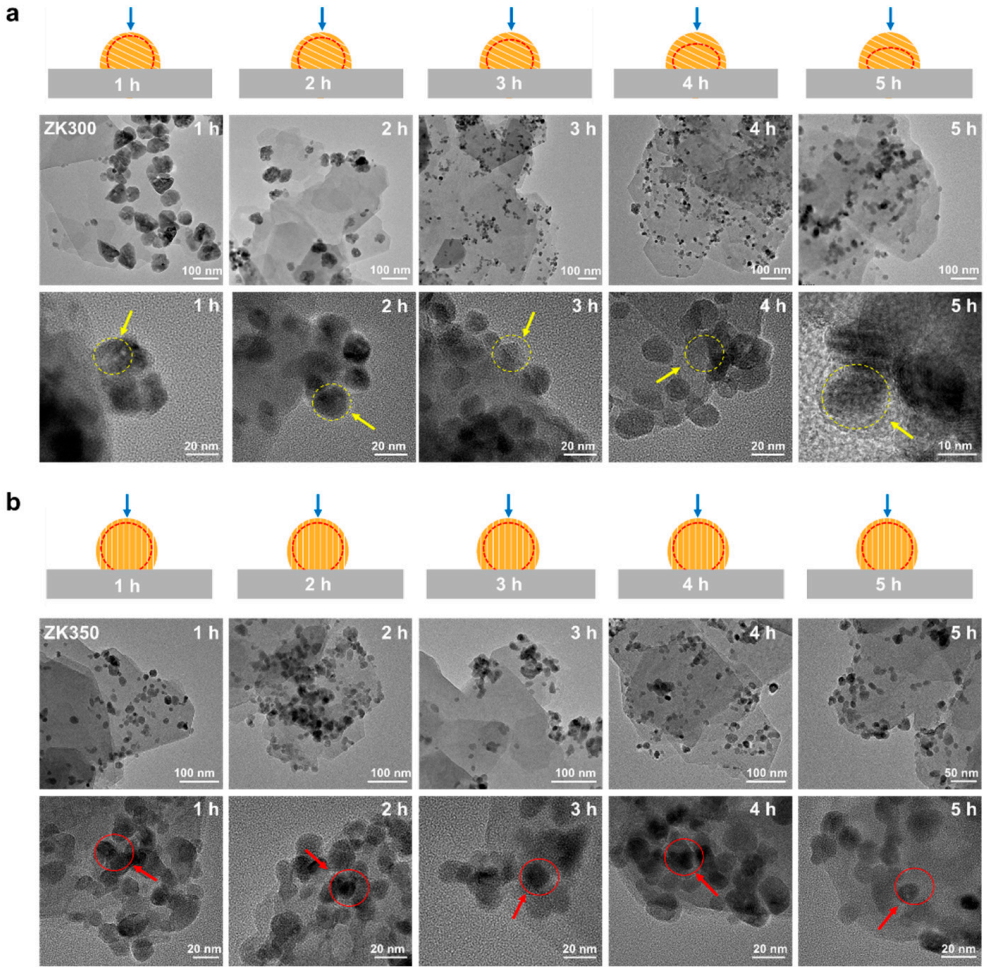

Figure 3. HRTEM images of (**a**) ZK300 and (**b**) ZK350 after dissolution at 1 h, 2 h, 3 h, 4 h, and 5 h, respectively.

3.5. Antibacterial Activity Evaluation

The oxidative species, zinc ions, and electron transfer between the surface and bacteria are responsible for the antibacterial activities of ZnO; however, these species can all be affected by the oxygen vacancies, crystal planes, and surface activities when materials are exposed to the solution [28,47,48]. Zinc ions are toxic to bacteria because they can bind to the bacterial membrane and affect its metabolism. ZK250 and ZK300 exhibit higher concentration of zinc ions, and the concentration of zinc ions decreases with dihydroxylation of samples after exposure to the solution (Figure 4a). ZK350 and ZK400 display the lowest zinc ion concentration at all times. These results indicate that hydroxyl groups on the surface of the support can promote the dissolution of zinc oxide nanoparticles.

The oxidative species rely on the surface oxygen vacancies, and the dissolution of zinc oxide nanoparticles relies on the crystal structure and morphology of the nanoparticles. Electron transfer relies on the electrical chemical properties of the surface [8,49]. Herein, the antibacterial species were systematically investigated over ZnO/kaolinite samples to correlate the interface interactions induced by dehydroxylation and the antibacterial activities. The production of O_2^- and •OH was evaluated, showing that the intensity increases with time (Figures 4b and S12). ZK350 has a higher production of superoxide O_2^- at all timepoints, but there is no obvious difference between the other samples. ZK350 exhibits a higher yield of hydroxyl radical while ZK250 is the lowest compared with other samples. Furthermore, ZK350 has a higher yield of superoxide anion at all time points, and there is no obvious difference between the other samples.

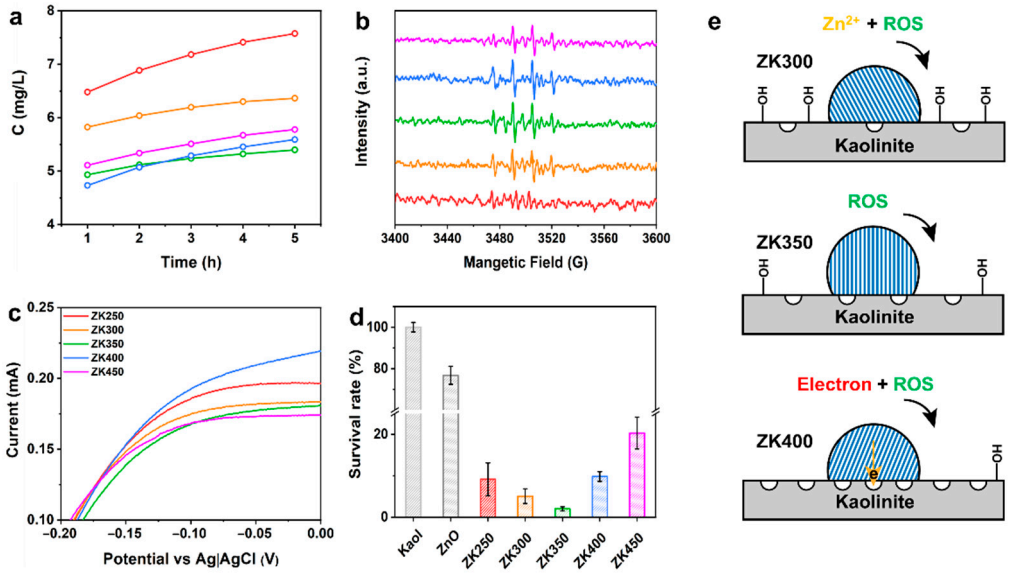

Figure 4. Evaluation of antibacterial activity. (**a**) Zinc ions released from samples at 1 h, 2 h, 3 h, 4 h, and 5 h; (**b**) Detection of •OH after prepared samples incubated in solution at 4 h; (**c**) I–V curves of a complex of bacteria and samples after 4 h; (**d**) Survival rate of samples; (**e**) Illustration of antibacterial mechanism of different interface interactions.

Extracellular electron transfer between the surface and the bacteria is a crucial step in antibacterial activities [50–52]. Cyclic voltammetry (CV) was conducted after incubation of materials and bacteria to further investigate the mechanism of current generation [53–55]. Figure S13 shows that the mixture of bacteria and materials exhibits a significant reduction reaction peak at −0.72 V, thus indicating that the electrons transfer from the bacteria membrane to the surface of the ZnO/kaolinite. ZK400 and ZK250 exhibit the higher current, indicating that the oxygen vacancies and hydroxyl groups on the kaolinite surface are all beneficial to the enhancement of current (Figure 4c). By contrast, ZK350 has the lowest current of all samples. Figure 4e summarizes the impact of ROS, zinc ions, and electron transfer on the antibacterial activities of the samples. ZK300 and ZK400 exhibit high antibacterial activities; they kill 95% and 90% of *E. coli*, respectively. ZK350 kills 98% of *E. coli*. ZK250 and ZK450 exhibit higher antibacterial activity versus ZK300 (Figures 4d, S14 and S15).

The oxidative species, zinc ions, and electron transfer between the surface and bacteria are responsible for the antibacterial activities of ZnO. These results demonstrate that the oxidative species, the dissolution of zinc oxide nanoparticles, and electron transfer rely on the (0001) Zn-polar surface of the zinc oxide nanoparticles. The remarkably different antibacterial activities can be attributed to (0001) Zn-polar surface of zinc oxide nanoparticles when the materials are exposed to solution. Therefore, the zinc oxide–support interaction has significant effects on the morphology, size, crystal lattice distance, and crystal orientation, resulting in different antibacterial mechanisms (Figure S16). ZnO nanoparticles preferentially grow along the <0001> direction with the terminal Zn-polar (0001) for ZK350. The (0001) Zn-polar surface exposed on the surface of ZnO nanoparticles is considered to be the effective antibacterial surface, which is determined by the interfacial interactions. These data further reveal that the interfacial interactions induced by dehydroxylation affect the zinc oxide nanoparticle Zn-polar (0001) surface, which, in turn, determines the antibacterial activity. Only the oxidative species were produced and exhibited the highest antibacterial activity when the interface interactions were too strong. The intensity of interactions between zinc oxide nanoparticles and supports could promote zinc ion leaching, reactive oxygen species and electron transfer, which plays a major role in the antibacterial activity and affect the antibacterial performance of zinc oxide nanoparticles.

4. Conclusions

In summary, this strategy can tune metal oxide–kaolinite interactions through dehydroxylation. The morphology, crystal lattice distance, and crystal orientation were constructed with the greater exposure of the ZnO active (0001) Zn-polar surface. The zinc oxide nanoparticles–kaolinite interaction induced by dehydroxylation was because the surface of kaolinite exhibits different surface free energies—especially polar surface free energy γ^{AB}, i.e., the electronic receptivity that could strengthen the zinc oxide–kaolinite interaction. The antibacterial activities of the samples exhibit a similar trend for surface free energy. These results demonstrate that the highest surface free energy of the kaolinite surface results in higher interfacial interactions of zinc oxide–support, which could increase the proportion of the (0001) Zn-polar surface and promote the production of reactive oxygen species, electron transfer, and leaching zinc ion. Our results can help circumvent the current limits of approaches involving strong chemical reagents while concurrently obtaining various nano structural zinc oxide nanoparticles, which could lead to opportunities to rationally maneuver structure dependent biomedical outcomes.

Supplementary Materials: The following supporting information can be downloaded at: https://www.mdpi.com/article/10.3390/min12091097/s1, Figure S1: Schematic illustration of the interaction formation between ZnO and support; Figure S2: TG and DSC curve of kaolinite; Figure S3: FTIR spectra of samples; Figure S4: XRD pattern of samples; Figure S5: XRD pattern of ZK500; Figure S6: SEM images of ZK500 and white line represent the zinc oxide nanoparticles; Figure S7: Schematic illustration of ZnO nanoparticles on the kaolinite support; Figure S8: Heights of samples measured by AFM; Figure S9: XPS spectra of Al, Si, O, and Zn of all samples; Figure S10: Lifshitz–van der Waals free energy and Lewis base surface free energy; Figure S11: STEM images; Figure S12: Detection of superoxide ion after prepared samples incubated in solution at 1 h, 2 h, 3 h, and 4 h; Figure S13: C-V curves of a complex of bacteria and samples after 4 h; Figure S14: SEM images of ZK300 and ZK350 incubated with bacteria; Figure S15: Physiological changes in bacteria incubated with samples, ZK300, and ZK350 compared with control; Figure S16: Schematic illustration of the interfacial interactions on antibacterial activity; Table S1: Theoretical composition of kaolinite; Table S2: The composition of kaolinite samples; Table S3: Intensity ratio of I(100)/I(002); Table S4: The parameters of the surface free energy of liquids.

Author Contributions: H.Y. conceived the project. D.W. wrote initial drafts of the work. H.Y. wrote the final paper. D.W. and Y.M. designed the experiments, synthesized, and characterized the materials. D.W., Y.M., A.T. and H.Y. analyzed the data. All of the authors contributed to the scientific discussion. All authors have read and agreed to the published version of the manuscript.

Funding: This work was supported by the National Natural Science Foundation of China (52042403, 51974367), the CUG Scholar Scientific Research Funds at China University of Geosciences (Wuhan) (2019152), and Hunan Provincial Innovation Foundation for Postgraduates (CX20190137).

Data Availability Statement: The data presented in this study are available on request from the corresponding author.

Conflicts of Interest: The authors declare no conflict of interest.

References

1. Mishra, Y.K.; Adelung, R. ZnO tetrapod materials for functional applications. *Mater. Today* **2018**, *21*, 631–651. [CrossRef]
2. Jin, Y.; Long, J.; Ma, X.; Zhou, T.; Zhang, Z.; Lin, H.; Long, J.; Wang, X. Synthesis of caged iodine-modified ZnO nanomaterials and study on their visible light photocatalytic antibacterial properties. *Appl. Catal. B Environ.* **2019**, *256*, 117873. [CrossRef]
3. Volkov, V.V.; Oliver, D.J.; Perry, C.C. Polariton condensation and surface enhanced Raman in spherical ZnO microcrystals. *Nat. Commun.* **2020**, *11*, 4908. [CrossRef]
4. Mishra, P.K.; Mishra, H.; Ekielski, A.; Talegaonkar, S.; Vaidya, B. Zinc oxide nanoparticles: A promising nanomaterial for biomedical applications. *Drug Discov. Today* **2017**, *22*, 1825–1834. [CrossRef]
5. Podporska-Carroll, J.; Myles, A.; Quilty, B.; McCormack, D.E.; Fagan, R.; Hinder, S.J.; Dionysiou, D.D.; Pillai, S.C. Antibacterial properties of F-doped ZnO visible light photocatalyst. *J. Hazard. Mater.* **2017**, *324*, 39–47. [CrossRef] [PubMed]
6. Wang, D.; Lin, Z.; Wang, T.; Yao, Z.; Qin, M.; Zheng, S.; Lu, W. Where does the toxicity of metal oxide nanoparticles come from: The nanoparticles, the ions, or a combination of both? *J. Hazard. Mater.* **2016**, *308*, 328–334. [CrossRef] [PubMed]

7. Jiang, C.; Aiken, G.R.; Hsu-Kim, H. Effects of Natural Organic Matter Properties on the Dissolution Kinetics of Zinc Oxide Nanoparticles. *Environ. Sci. Technol.* **2015**, *49*, 11476–11484. [CrossRef]
8. Ruiz Puigdollers, A.; Schlexer, P.; Tosoni, S.; Pacchioni, G. Increasing Oxide Reducibility: The Role of Metal/Oxide Interfaces in the Formation of Oxygen Vacancies. *ACS Catal.* **2017**, *7*, 6493–6513. [CrossRef]
9. Parastaev, A.; Muravev, V.; Huertas Osta, E.; van Hoof, A.J.F.; Kimpel, T.F.; Kosinov, N.; Hensen, E.J.M. Boosting CO_2 hydrogenation via size-dependent metal–support interactions in cobalt/ceria-based catalysts. *Nat. Catal.* **2020**, *3*, 526–533. [CrossRef]
10. Jiang, J.; Pi, J.; Cai, J. The Advancing of Zinc Oxide Nanoparticles for Biomedical Applications. *Bioinorg. Chem. Appl.* **2018**, *2018*, 1062562. [CrossRef]
11. Dong, J.; Fu, Q.; Li, H.; Xiao, J.; Yang, B.; Zhang, B.; Bai, Y.; Song, T.; Zhang, R.; Gao, L.; et al. Reaction-Induced Strong Metal-Support Interactions between Metals and Inert Boron Nitride Nanosheets. *J. Am. Chem. Soc.* **2020**, *142*, 17167–17174. [CrossRef] [PubMed]
12. Binninger, T. Electronic metal-support interactions in vacuum vs. electrolyte. *Nat. Commun.* **2020**, *11*, 1471. [CrossRef] [PubMed]
13. Shan, J.; Li, X.; Yang, K.; Xiu, W.; Wen, Q.; Zhang, Y.; Yuwen, L.; Weng, L.; Teng, Z.; Wang, L. Efficient Bacteria Killing by Cu_2WS_4 Nanocrystals with Enzyme-like Properties and Bacteria-Binding Ability. *ACS Nano* **2019**, *13*, 13797–13808. [CrossRef] [PubMed]
14. Beck, A.; Huang, X.; Artiglia, L.; Zabilskiy, M.; Wang, X.; Rzepka, P.; Palagin, D.; Willinger, M.G.; van Bokhoven, J.A. The dynamics of overlayer formation on catalyst nanoparticles and strong metal-support interaction. *Nat. Commun.* **2020**, *11*, 3220. [CrossRef]
15. van Deelen, T.W.; Hernández Mejía, C.; de Jong, K.P. Control of metal-support interactions in heterogeneous catalysts to enhance activity and selectivity. *Nat. Catal.* **2019**, *2*, 955–970. [CrossRef]
16. Yoon, S.; Oh, K.; Liu, F.; Seo, J.H.; Somorjai, G.A.; Lee, J.H.; An, K. Specific Metal–Support Interactions between Nanoparticle Layers for Catalysts with Enhanced Methanol Oxidation Activity. *ACS Catal.* **2018**, *8*, 5391–5398. [CrossRef]
17. Guan, D.; Ryu, G.; Hu, Z.; Zhou, J.; Dong, C.L.; Huang, Y.C.; Zhang, K.; Zhong, Y.; Komarek, A.C.; Zhu, M.; et al. Utilizing ion leaching effects for achieving high oxygen-evolving performance on hybrid nanocomposite with self-optimized behaviors. *Nat. Commun.* **2020**, *11*, 3376. [CrossRef]
18. Campbell, C.T.; Mao, Z. Chemical Potential of Metal Atoms in Supported Nanoparticles: Dependence upon Particle Size and Support. *ACS Catal.* **2017**, *7*, 8460–8466. [CrossRef]
19. Jackson, C.; Smith, G.T.; Inwood, D.W.; Leach, A.S.; Whalley, P.S.; Callisti, M.; Polcar, T.; Russell, A.E.; Levecque, P.; Kramer, D. Electronic metal-support interaction enhanced oxygen reduction activity and stability of boron carbide supported platinum. *Nat. Commun.* **2017**, *8*, 15802. [CrossRef]
20. Hong, J.; Wang, B.; Xiao, G.; Wang, N.; Zhang, Y.; Khodakov, A.Y.; Li, J. Tuning the Metal–Support Interaction and Enhancing the Stability of Titania-Supported Cobalt Fischer–Tropsch Catalysts via Carbon Nitride Coating. *ACS Catal.* **2020**, *10*, 5554–5566. [CrossRef]
21. O'Connor, N.J.; Jonayat, A.S.M.; Janik, M.J.; Senftle, T.P. Interaction trends between single metal atoms and oxide supports identified with density functional theory and statistical learning. *Nat. Catal.* **2018**, *1*, 531–539. [CrossRef]
22. Sui, X.; Zhang, L.; Li, J.; Doyle-Davis, K.; Li, R.; Wang, Z.; Sun, X. Advanced Support Materials and Interactions for Atomically Dispersed Noble-Metal Catalysts: From Support Effects to Design Strategies. *Adv. Energy Mater.* **2021**, *7*, 2102556. [CrossRef]
23. Pan, L.; Liu, Y.T.; Zhong, M.; Xie, X.M. Coordination-Driven Hierarchical Assembly of Hybrid Nanostructures Based on 2D Materials. *Small* **2020**, *16*, e1902779. [CrossRef] [PubMed]
24. Lang, R.; Du, X.; Huang, Y.; Jiang, X.; Zhang, Q.; Guo, Y.; Liu, K.; Qiao, B.; Wang, A.; Zhang, T. Single-Atom Catalysts Based on the Metal-Oxide Interaction. *Chem. Rev.* **2020**, *120*, 11986–12043. [CrossRef]
25. Qin, R.; Liu, P.; Fu, G.; Zheng, N. Strategies for Stabilizing Atomically Dispersed Metal Catalysts. *Small Methods* **2018**, *2*, 1700286. [CrossRef]
26. Mentasty, L.R.; Gorriz, O.F.; Cadus, L.E. Chromium oxide supported on different Al_2O_3 supports: Catalytic propane dehydrogenation. *Ind. Eng. Chem. Res.* **1999**, *38*, 396–404. [CrossRef]
27. Feng, X.; Yan, Y.; Wan, B.; Li, W.; Jaisi, D.P.; Zheng, L.; Zhang, J.; Liu, F. Enhanced Dissolution and Transformation of ZnO Nanoparticles: The Role of Inositol Hexakisphosphate. *Environ. Sci. Technol.* **2016**, *50*, 5651–5660. [CrossRef]
28. Lakshmi Prasanna, V.; Vijayaraghavan, R. Insight into the Mechanism of Antibacterial Activity of ZnO: Surface Defects Mediated Reactive Oxygen Species Even in the Dark. *Langmuir* **2015**, *31*, 9155–9162. [CrossRef]
29. Mudunkotuwa, I.A.; Rupasinghe, T.; Wu, C.M.; Grassian, V.H. Dissolution of ZnO nanoparticles at circumneutral pH: A study of size effects in the presence and absence of citric acid. *Langmuir* **2012**, *28*, 396–403. [CrossRef]
30. Zhan, J.; Chen, H.; Zhou, H.; Hao, L.; Xu, H.; Zhou, X. Mt-supported ZnO/TiO_2 nanocomposite for agricultural antibacterial agent involving enhanced antibacterial activity and increased wettability. *Appl. Clay Sci.* **2021**, *214*, 1700286. [CrossRef]
31. Dong, X.; Ren, B.; Sun, Z.; Li, C.; Zhang, X.; Kong, M.; Zheng, S.; Dionysiou, D.D. Monodispersed $CuFe_2O_4$ nanoparticles anchored on natural kaolinite as highly efficient peroxymonosulfate catalyst for bisphenol A degradation. *Appl. Catal. B Environ.* **2019**, *253*, 206–217. [CrossRef]
32. Eudier, F.; Savary, G.; Grisel, M.; Picard, C. Skin surface physico-chemistry: Characteristics, methods of measurement, influencing factors and future developments. *Adv. Colloid Interface Sci.* **2019**, *264*, 11–27. [CrossRef] [PubMed]
33. Gusnaniar, N.; van der Mei, H.C.; Qu, W.; Nuryastuti, T.; Hooymans, J.M.M.; Sjollema, J.; Busscher, H.J. Physico-chemistry of bacterial transmission versus adhesion. *Adv. Colloid Interface Sci.* **2017**, *250*, 15–24. [CrossRef] [PubMed]

34. Li, W.Z.; Kovarik, L.; Mei, D.; Liu, J.; Wang, Y.; Peden, C.H. Stable platinum nanoparticles on specific $MgAl_2O_4$ spinel facets at high temperatures in oxidizing atmospheres. *Nat. Commun.* **2013**, *4*, 2481. [CrossRef]
35. Kim, J.-H.; Woo, H.; Choi, J.; Jung, H.-W.; Kim, Y.-T. CO_2 Electroreduction on Au/TiC: Enhanced Activity Due to Metal–Support Interaction. *ACS Catal.* **2017**, *7*, 2101–2106. [CrossRef]
36. Jiang, Z.; Jing, M.; Feng, X.; Xiong, J.; He, C.; Douthwaite, M.; Zheng, L.; Song, W.; Liu, J.; Qu, Z. Stabilizing platinum atoms on CeO_2 oxygen vacancies by metal-support interaction induced interface distortion: Mechanism and application. *Appl. Catal. B Environ.* **2020**, *278*, 119304. [CrossRef]
37. Gao, Y.; Zhao, Y.; Li, Y.C.; Huang, Q.; Mallouk, T.E.; Wang, D. Interfacial Chemistry Regulation via a Skin-Grafting Strategy Enables High-Performance Lithium-Metal Batteries. *J. Am. Chem. Soc.* **2017**, *139*, 15288–15291. [CrossRef]
38. Perazzolo, V.; Brandiele, R.; Durante, C.; Zerbetto, M.; Causin, V.; Rizzi, G.A.; Cerri, I.; Granozzi, G.; Gennaro, A. Density Functional Theory (DFT) and Experimental Evidences of Metal–Support Interaction in Platinum Nanoparticles Supported on Nitrogen- and Sulfur-Doped Mesoporous Carbons: Synthesis, Activity, and Stability. *ACS Catal.* **2018**, *8*, 1122–1137. [CrossRef]
39. Preedy, E.; Perni, S.; Nipic, D.; Bohinc, K.; Prokopovich, P. Surface roughness mediated adhesion forces between borosilicate glass and gram-positive bacteria. *Langmuir* **2014**, *30*, 9466–9476. [CrossRef]
40. Tian, S.; Gong, W.; Chen, W.; Lin, N.; Zhu, Y.; Feng, Q.; Xu, Q.; Fu, Q.; Chen, C.; Luo, J.; et al. Regulating the Catalytic Performance of Single-Atomic-Site Ir Catalyst for Biomass Conversion by Metal–Support Interactions. *ACS Catal.* **2019**, *9*, 5223–5230. [CrossRef]
41. Li, J.; Lin, Y.; Pan, X.; Miao, D.; Ding, D.; Cui, Y.; Dong, J.; Bao, X. Enhanced CO_2 Methanation Activity of Ni/Anatase Catalyst by Tuning Strong Metal–Support Interactions. *ACS Catal.* **2019**, *9*, 6342–6348. [CrossRef]
42. Tang, H.L.; Su, Y.; Zhang, B.S.; Lee, A.F.; Isaacs, M.A.; Wilson, K.; Li, L.; Ren, Y.G.; Huang, J.H.; Haruta, M.; et al. Classical strong metal-support interactions between gold nanoparticles and titanium dioxide. *Sci. Adv.* **2017**, *3*, 8. [CrossRef] [PubMed]
43. Hou, Y.; Aydin, E.; De Bastiani, M.; Xiao, C.X.; Isikgor, F.H.; Xue, D.J.; Chen, B.; Chen, H.; Bahrami, B.; Chowdhury, A.H.; et al. Efficient tandem solar cells with solution-processed perovskite on textured crystalline silicon. *Science* **2020**, *367*, 1135–1140. [CrossRef] [PubMed]
44. Lin, S.; Zheng, M.; Luo, J.; Wang, Z.L. Effects of Surface Functional Groups on Electron Transfer at Liquid-Solid Interfacial Contact Electrification. *ACS Nano* **2020**, *14*, 10733–10741. [CrossRef]
45. Tao, Y.; Ju, E.; Ren, J.; Qu, X. Bifunctionalized mesoporous silica-supported gold nanoparticles: Intrinsic oxidase and peroxidase catalytic activities for antibacterial applications. *Adv. Mater.* **2015**, *27*, 1097–1104. [CrossRef]
46. Sirelkhatim, A.; Mahmud, S.; Seeni, A.; Kaus, N.H.M.; Ann, L.C.; Bakhori, S.K.M.; Hasan, H.; Mohamad, D. Review on Zinc Oxide Nanoparticles: Antibacterial Activity and Toxicity Mechanism. *Nanomicro Lett* **2015**, *7*, 219–242. [CrossRef]
47. Applerot, G.; Lipovsky, A.; Dror, R.; Perkas, N.; Nitzan, Y.; Lubart, R.; Gedanken, A. Enhanced Antibacterial Activity of Nanocrystalline ZnO Due to Increased ROS-Mediated Cell Injury. *Adv. Funct. Mater.* **2009**, *19*, 842–852. [CrossRef]
48. Wang, Y.; Xie, Y.; Li, J.; Peng, Z.H.; Sheinin, Y.; Zhou, J.; Oupicky, D. Tumor-Penetrating Nanoparticles for Enhanced Anticancer Activity of Combined Photodynamic and Hypoxia-Activated Therapy. *ACS Nano* **2017**, *11*, 2227–2238. [CrossRef]
49. Abdal Dayem, A.; Hossain, M.K.; Lee, S.B.; Kim, K.; Saha, S.K.; Yang, G.M.; Choi, H.Y.; Cho, S.G. The Role of Reactive Oxygen Species (ROS) in the Biological Activities of Metallic Nanoparticles. *Int. J. Mol. Sci.* **2017**, *18*, 120. [CrossRef]
50. Yang, M.Q.; Xu, Y.J.; Lu, W.; Zeng, K.; Zhu, H.; Xu, Q.H.; Ho, G.W. Self-surface charge exfoliation and electrostatically coordinated 2D hetero-layered hybrids. *Nat. Commun.* **2017**, *8*, 14224. [CrossRef]
51. Furst, A.L.; Francis, M.B. Impedance-Based Detection of Bacteria. *Chem. Rev.* **2019**, *119*, 700–726. [CrossRef] [PubMed]
52. Wang, R.; Xue, J.J.; Wang, K.L.; Wang, Z.K.; Luo, Y.Q.; Fenning, D.; Xu, G.W.; Nuryyeva, S.; Huang, T.Y.; Zhao, Y.P.; et al. Constructive molecular configurations for surface-defect passivation of perovskite photovoltaics. *Science* **2019**, *366*, 1509–1513. [CrossRef]
53. Jiang, X.; Wang, F.; Wei, Q.; Li, H.; Shang, Y.; Zhou, W.; Wang, C.; Cheng, P.; Chen, Q.; Chen, L.; et al. Ultra-high open-circuit voltage of tin perovskite solar cells via an electron transporting layer design. *Nat. Commun.* **2020**, *11*, 1245. [CrossRef] [PubMed]
54. Zhou, S.; Tang, J.; Yuan, Y.; Yang, G.; Xing, B. TiO_2 Nanoparticle-Induced Nanowire Formation Facilitates Extracellular Electron Transfer. *Environ. Sci. Technol. Lett.* **2018**, *5*, 564–570. [CrossRef]
55. Wang, G.; Feng, H.; Hu, L.; Jin, W.; Hao, Q.; Gao, A.; Peng, X.; Li, W.; Wong, K.Y.; Wang, H.; et al. An antibacterial platform based on capacitive carbon-doped TiO_2 nanotubes after direct or alternating current charging. *Nat. Commun.* **2018**, *9*, 2055. [CrossRef] [PubMed]